Materials & Design 224 (2022) 111323

Contents lists available at ScienceDirect

Materials & Design

journal homepage: www.elsevier.com/locate/matdes

On the interplay between microstructure, residual stress and fracture toughness of (Hf-Nb-Ta-Zr)C multi-metal carbide hard coatings

Hariprasad Gopalan [a,*,1], Amalraj Marshal [b,2], Marcus Hans [b], Daniel Primetzhofer [c], Niels Cautaerts [a], Benjamin Breitbach [a], Bernhard Völker [a,b,d], Christoph Kirchlechner [a,e], Jochen M. Schneider [b], Gerhard Dehm [a]

[a] Max Planck Institut für Eisenforschung, Düsseldorf, Germany
[b] Materials Chemistry, RWTH Aachen University, Aachen, Germany
[c] Department of Physics and Astronomy, Uppsala University, Uppsala, Sweden
[d] Materials Center Leoben, Leoben, Austria
[e] Institute for Applied Materials, Karlsruhe Institute of Technology, Karlsruhe, Germany

HIGHLIGHTS

- Multi-element (HfNbTaZr)C coatings obtained with near super hardness and respectable toughness.
- The coating mechanical properties such as hardness, strength and fracture toughness degrade with increasing deposition temperatures, contrary to expectation.
- The coarsening of the excess carbon rich phase at grain boundaries with increasing deposition temperature is speculated to be responsible for degradation of mechanical properties.
- Cube corner nanoindentation crack profile is sensitive to residual stress.
- True nanoindentation toughness measurements agree very well with *in situ* SEM based microcantilever fracture toughness testing.

GRAPHICAL ABSTRACT

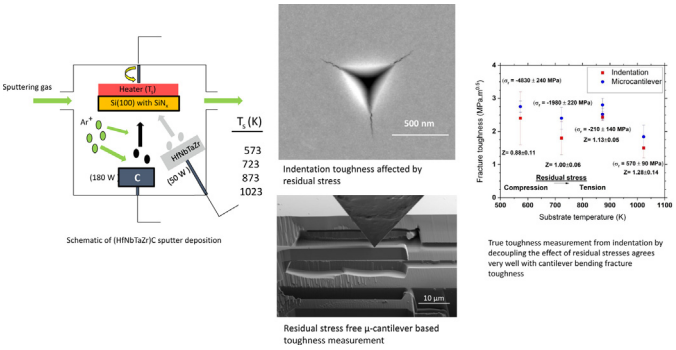

ARTICLE INFO

Article history:
Received 25 April 2022
Revised 3 October 2022
Accepted 26 October 2022
Available online 27 October 2022

Keywords:
High entropy ceramics
DC sputtering
Fracture toughness
Residual stress
Nanoindentation

ABSTRACT

The development of sputtered coatings with improved hardness-toughness property combination is widely sought after. Multi-element ceramic carbide (Hf-Nb-Ta-Zr)C coatings with excess carbon, synthesized by DC co-sputtering is presented in this study as a promising candidate to achieve this objective. The specific roles of microstructure and residual stress are decoupled in order to understand their influence on the mechanical properties. Extensive mechanical characterization through *in situ* testing of focused ion beam fabricated microcantilevers and nanoindentation based approaches are adopted to quantitatively separate the effect of residual stresses on the fracture toughness of the (Hf-Nb-Ta-Zr)C coatings. Residual stress free, microcantilever testing in notched and unnotched conditions, in combination with microstructural characterization unambiguously reveals the intrinsic mechanical behavior of coatings, which solely depend on the microstructure. On the other hand, nanoindentation based testing techniques probe the influence of residual stress and microstructure on the measured mechanical

* Corresponding author.
E-mail addresses: h.gopalan@mpie.de, hariprasad.gopalan@kit.edu (H. Gopalan).
[1] Present address: Institute for Applied Materials(FML), Karlsruhe Institute of Technology, Karlsruhe, Germany.
[2] Present address: IM2NP - UMR 7334, Faculté des Sciences de Saint-Jérôme, Marseille, France.

https://doi.org/10.1016/j.matdes.2022.111323

properties. The segregation and thickening of carbon-rich clusters, especially to the grain boundaries with increasing deposition temperatures is speculated to lead to substantial degradation in all mechanical properties measured. An easier fracture path through grain boundaries leads to a reduction in fracture resistance, which is possibly related to carbon enrichment.

1. Introduction

Transition metal carbides have interesting properties including high hardness [1,2], elastic modulus of up to 500 GPa [2], electrical conductivity of up to 5×10^6 S/m [3] and modest fracture toughness values on the order of 2–3 MPa $m^{0.5}$ [2]. Therefore, in their thin film form, they find a variety of applications such as hard coatings for tools, heat resistant coatings, barrier layers for high temperature electronics and as catalytic/electrode materials for electrochemical systems [4–6]. The presence of excess free carbon in some of these transition metal carbides reduces the friction coefficient significantly, thereby making them attractive for tribological applications, without significantly affecting properties such as hardness and modulus [7]. Recently, several studies have emerged on ceramic systems [8], taking inspiration from high entropy/compositionally complex alloys in the metals literature [9–11]. The hard coating community has also embraced this new development with enthusiasm and a variety of borides, carbides and nitrides and combinations thereof have been synthesized [12–14]. The fundamental concept underlying this new multi-element alloy development strategy, *the high entropy effect* remains under intense debate in the metals community [11]. A direct extension to ceramic systems pose significant difficulty, for example, Kirnbauer *et al.* [15,16] point out that only the metal sub-lattice is expected to contribute to the configuration entropy. Despite some of these limitations, the pace of ceramic thin film materials development advertising the so called "high entropy effect" appears to be accelerating. A part of this allurement is technological, as some of these multi-element ceramic coatings show an excellent promise towards attaining super-hardness (H > 40 GPa) [17,18]. From an application perspective, attaining respectable fracture toughness values is equally important. The quest for materials with improved hardness-toughness trade-off have to rely largely on trial and error [19] or be motivated by shear flow prediction with *ab initio* calculations on complex crystal structures [20]. Ceramics with the metal sub-lattice populated with a multi-metal combination, offer new avenues for exploring these conflicting property combinations. For example, Malinovskis *et al.* [21] have shown that (CrNbTaTiW)C thin films show improved hardness and corrosion resistance. Fritze *et al.* [22] have shown that the addition of carbon to metallic multicomponent coatings lead to improvement in indentation cracking resistance. Furthermore, Hossain *et al.* [23] have recently investigated the effects of carbon stoichiometry on the hardness, modulus and indentation yield strengths of sputter deposited (HfNbTaTiZr)C films. To the best of the authors' knowledge, no reports exist yet, which have investigated the fracture toughness of sputter deposited multi-metal carbide coatings. For studying mechanical properties of hard coatings, nanoindentation remains popular due to its relative ease of use and availability. In addition to determining hardness and reduced modulus, the technique can be used to deduce fracture toughness estimates. However, few experimental studies have successfully used nanoindentation techniques to determine fracture toughness of the hard coating systems [20,24–26]. Furthermore, sputter deposited coatings often have significant residual stresses. Decoupling the role of residual stresses on the intrinsic toughness of coatings on the microscale is important, so that they may be used to favorably leverage overall coating response. Towards realizing this end, we synthesized multi-metal carbide (Hf-Nb-Ta-Zr)C films with a carbon excess at different substrate temperatures, and characterized their microstructural and mechanical performance. The metallic elements were chosen based on their strong affinity to form monocarbides [27]. With the lessons learnt from this study, we highlight directions for designing and testing approach for multi-metal ceramic coatings. .

2. Experimental methods and background

2.1. Thin film deposition

The thin film deposition was carried out in a laboratory scale magnetron sputtering chamber with a base pressure < 1×10^{-5} Pa. Si (100) substrates with an additional 50 nm silicon nitride, which is a strong diffusion barrier layer up to 1373 K [28]. This is done to minimize the possibility of interfacial reactions between substrate and film materials. The Substrate was placed on a substrate holder with a halogen lamp heater. A pyrolytic graphite target from Kurt J. Lesker® (purity 99.999%) as well as an equimolar $Hf_{25}Nb_{25}Ta_{25}Zr_{25}$ target (Plansee Composite Materials GmbH, purity 99.9%) were used in a co-sputtering setup at 0 and 45°, respectively, with respect to the substrate holder and the target-to-substrate distance was 10 cm. Growth temperatures of 573, 723, 873 and 1023 K were employed based on a temperature calibration using a thermocouple. The venting temperature was < 353 K to minimize surface chemistry modifications [29]. Substrate rotation was used for synthesis of thin films with homogeneous composition and Ar was introduced at a deposition pressure of 0.4 Pa. The graphite and $Hf_{25}Nb_{25}Ta_{25}Zr_{25}$ targets were operated at 180 W (DC power supply) and 50 W (DC power supply), respectively. The deposition time was 5 h to obtain a film thickness of at least 3 μm.

2.2. X-ray characterization

X-ray investigations for phase analysis, texture and residual stress measurements were carried out in a Seifert THETA-THETA X-ray diffractometer. The diffractometer was equipped with a cobalt source (wavelength Kα = 1.789 Å), a polycapillary beam optic, a 4- circle goniometer and an energy dispersive point detector. The θ-2 θ measurements were carried out with a step size of $\Delta 2\theta = 0.03°$ and a count time of 10 s/step. To avoid X-ray reflections from the substrate a θ- offset of the incoming beam was kept at 5°. The pole figure measurements were carried out with (111),(200) and (220) reflections. The in-plane rotation angle ϕ covered a range from 0 to 360° and the out of plane tilt angle ψ had a range of 0-85°, both had a step size of 5°. The count time was kept at 3 s. The texture data was processed through MATLAB toolbox MTEX [30]. The residual stress was obtained with the $\sin^2\psi$ method. An angular step size of $\Delta 2 = 0.1°$ was used with a count time of 3 s per step. Two orthogonal in plane angles $\phi = 0°$ and 90° were used and the out of plane tilt angle ψ was varied from −60° to

60° with 9 steps in-between. The (420) reflection was fixed for the residual stress estimation. The lattice parameter determined for the reflection across different ψ angles is plotted against the corresponding $\sin^2\psi$ and fitted with linear regression to estimate the residual stress [31]. The material was assumed to possess isotropic elastic properties with an elastic modulus E = 550 GPa and a Poisson's ratio $\upsilon = 0.2$, based on rule of mixtures of the constituent monocarbides [32,33]. The residual stress reported is the average of the two measured values for the two orthogonal in-plane angles, ϕ = 0° and 90°. The linear coefficient of thermal expansion (CTE) was obtained by *in situ* X-ray diffraction for a thin film grown at 873 K with an Anton Paar Hot Domed Stage (DHS 1000) inside a Bruker AXS D8 General Area Detection Diffraction System. While the dome was evacuated to 6×10^{-1} Pa, the film surface temperature was increased to 570 °C and monitored with a thermocouple. The stress-free lattice parameters were determined from (220) lattice planes in Bragg-Brentano geometry, using the $\sin^2\psi$ method and a linear fit was used for determining the CTE.

2.3. Chemical and microstructural characterization

The chemical composition of the coatings deposited at different temperatures was characterized by energy dispersive spectroscopy (EDS) with an electron accelerating voltage of 15 kV housed in a dual beam electron and focused ion beam (FIB), Zeiss-Auriga microscope. In addition, the chemical composition of the thin film grown at 873 K was quantified by time-of-flight elastic recoil detection analysis (ERDA) at the tandem accelerator laboratory of Uppsala University. Target recoils were created using projectiles of $^{127}I^{8+}$ ions with 36 MeV primary energy. Depth-resolved chemical compositions were obtained from time-energy coincidence spectra of the recoils recorded using a time-of-flight telescope in 45°forward direction with respect to the axis of the incident beam [34]. Data conversion to depth profiles was done using the CONTES software package [35]. While the statistic uncertainties for concentrations of the elements are provided in Table 1, systematic uncertainties of up to 10 % relative deviation can be expected for carbon. This estimate is based on the following two main sources of uncertainty: at first, the employed time-of-flight telescope has an efficiency which significantly deviates from unity for light species. The second contribution is a potential uncertainty in the specific energy loss of both projectile ion and recoil species, linearly entering the calculation of concentration depth profiles. From these factors, in combination, a smaller systematic deviation can be expected for heavier species. The limited mass resolution for heavy recoils requires that the sum of concentrations of Zr/Nb and Hf/Ta is determined by ERDA, while EDS is expected to provide reliable ratios of elements close to each other in atomic number.

Local chemical composition analysis at the nanometer scale was employed for thin films grown at 873 and 1023 K by three-dimensional atom probe tomography using a CAMECA LEAP 4000X HR with laser-assisted field evaporation. Needle-like specimens were prepared by focused ion beam in a FEI Helios Nanolab 660 dual-beam microscope according to a standard protocol [36]. About 1.4 million ions were obtained for the film grown at 873 K with 30 pJ laser pulse energy, 60 K base temperature and 1.0% detection rate. These parameters had to be changed for the film deposited at 1023 K since early fracture of the specimens was observed. One million ions were acquired at 100 pJ, 30 K and 0.5%. The laser pulse frequency was 125 kHz for both specimens and reconstructions were done with IVAS 3.8.0 using the shank angle protocol. Microstructural characterization was further carried out by transmission electron microscopy using a Titan Themis probe-corrected microscope (Thermo Fisher Scientific) operating at 300 kV. High angle annular dark field (HAADF) and energy dispersive X-ray spectroscopy (EDX) were employed in the scanning mode (STEM) to detect the distribution of the different elements. Samples were prepared by FIB lift out using a SCIOS 2 dual-beam instrument (Thermo Fisher) with a final cleaning step using an accelerating voltage of 2 kV for the Gallium ions.

2.4. Mechanical testing and related characterization

Nanoindentation measurements were performed in an Agilent G200 instrument. A Berkovich tip was employed to determine the hardness and elastic modulus by using the Oliver-Pharr method coupled with a continuous stiffness measurement (CSM), imposing a harmonic displacement of 2 nm and a frequency of 45 Hz. The elastic modulus is calculated by assuming a Poisson's ratio of 0.2 for the multinary carbide [33]. The maximum indentation depths were limited to below 10% (300 nm) of the coating thickness. At least 30 measurements were performed for each condition. Additionally, an equal number of quasistatic indentations were also performed to a total depth of 150 nm without adopting the CSM option, to ascertain if the procedure yielded reliable results. Indentation fracture toughness was obtained by probing the coatings with a cube corner indenter. The crack lengths emanating from the corner of the indents were imaged with a Zeiss-Gemini 500 field emission scanning electron microscope (SEM) operating at an accelerating voltage of 10 kV. The fracture toughness values were calculated as an average of 16 measurements based on the methodology established by Pharr and co-workers [37,38]. The equation for determining indentation fracture toughness (K_c) is:

$$K_c = \frac{0.0352}{(1-\upsilon)}(\cot\Psi)^{\frac{2}{3}}\left(\frac{E}{H}\right)^{\frac{1}{2}}\frac{P_{\max}}{c^{3/2}} \quad (1)$$

Where, υ is the Poisson's ratio, ψ is the indenter semi angle, E is the elastic modulus, H is the hardness, P_{max} is maximum load and c is the crack length measured from the center of the indent. FIB cross section of three indents for every deposition temperature was performed with a platinum protection layer. Low currents of 240 pA and 50 pA were used for sectioning to minimise the influence of re-deposition. The microcantilever specimens were fabricated using FIB milling. The coarse milling was performed in a FEI Helios plasma-FIB using a Xenon source with a milling current of 15nA. Subsequently a Zeiss-Auriga Ga-ion FIB was employed with progressively lower currents from 4nA and 600 pA to facilitate a fine finish. The ion beam accelerating voltage was 30 kV for both machines. A total of 44 cantilevers were fabricated to determine elastic and fracture properties. 4 unnotched microcantilevers were prepared for each deposition temperature, to determine the elastic properties and the bending fracture strength. Similarly, to obtain the fracture toughness of the coatings, at least 6 notched cantilevers were fabricated for each deposition temperature. A through notch was fabricated with a milling current of 50 pA. In order to avoid the effects of *overfibbing* [39], a bridged notch was first fabricated and progressively milled with a low current of 600 pA to eliminate the material bridges and yield a through thickness notch with a constant notch depth *a*. The microcantilevers were tested in an ASMEC UNAT, *in situ* SEM indenter attached with a diamond wedge tip (length ~ 10 μm). The displacement rate for mechanical testing was fixed at 20 nm/s. Elastic modulus and bending fracture strength were determined from elementary beam theory assuming linear elastic material response for the unnotched cantilevers, the expressions employed are shown below.

$$E = \frac{4P}{hB}\left(\frac{L}{W}\right)^3 \quad (2)$$

$$\sigma_f = \frac{6P_{max}L}{BW^2} \quad (3)$$

Where, E is the elastic modulus, σ_f is the fracture strength, P is the load, h is the orresponding displacement, B, L and W correspond to the geometric dimensions width, length and the height of the cantilever. The width and the height of the microcantilevers had nominal dimensions of (3.0–3.5) μm, and their lengths were fixed at 5 times the height (15–16.5 μm). The notch depth, designated as a, was typically around 1 μm. The mode I fracture toughness, K_{Ic} shown below was determined based on linear elastic fracture mechanics and by finite element based numerical solutions for the geometric factor derived by Matoy *et al.* [39–41]

$$K_{Ic} = \frac{P_{max}L}{BW^{1.5}}\{1.46 + 24.36(\frac{a}{W}) - 47.21(\frac{a}{W})^2 + 75.18(\frac{a}{W})^3\} \quad (4)$$

3. Results and interpretation:

3.1. Crystallographic structure, residual stress and thermal expansion measurements

The X-ray diffraction data of the multi-metal carbide, shown in Fig. 1a, provides evidence that all deposited coatings were crystalline, and the peak positions agree with a B1 crystal structure (NaCl structure). The X-ray diffractograms have minor differences in the peak positions and the relative peak intensities. The broad X-ray peaks suggest a nanocrystalline microstructure. The lattice parameters calculated for the different deposition temperature are included in the supplementary table. The strong (111) (200) and (220) reflections point out towards a mixed fiber textures in films. The texture data as a function of deposition temperatures is provided in the supplementary section (fig. S2), confirms mixed fiber textures.

Additionally, residual stresses are expected to significantly depend on the growth temperature, while the other deposition parameters were kept constant. The residual stresses for coatings estimated by the $\sin^2\psi$ method (more details provided in supplementary section) are plotted as a function of growth temperature in Fig. 1b. At the lowest growth temperature (573 K), the residual stress is highly compressive with a value of −4830 ± 240 MPa, and with increasing temperature its magnitude decreases and eventually at 1023 K the residual stress becomes tensile (570 ± 90 MPa). In order to understand the influence of thermal stresses, the linear CTE was measured (shown in Fig. 1c), which had a value of 5.5 ± 0.3 × 10^{-6} K^{-1}. The quantification of the thermal contribution to residual stress and its role on the mechanical properties of the coatings will be discussed later in the manuscript. Optical micrographs (Supplementary fig. S2) corroborate the general trend of the residual stress evolution with growth temperature. For example, coating deposited at 1023 K shows a well-developed mud-cracking pattern indicative of high tensile residual stress present in the coating.

3.2. Microstructure and chemical composition

The chemical composition data is summarized in Table 1. The ERDA depth profile from the coating grown at 873 K reveals that the carbon concentration was 62 at.% , significantly higher than 50 at%, the highest stoichiometric value common in the cubic close packed carbide phase. EDS estimates for carbon composition are in the range of 64 to 66 at.% and likely affected by SEM chamber/surface contamination. Nevertheless, the EDS data can still be used for a relative comparison and provides Hf/Ta as well as Nb/Zr ratios. From the data it is clear that the chemical compositions of the coatings are not significantly affected by the growth temperature.

In order to understand the carbon overstoichiometry, local chemical composition analysis at the nanometer scale was performed and APT reconstructions from thin films grown at 873 and 1023 K are shown in Fig. 2.

While the metals appear to be homogeneously distributed, carbon-rich clusters with ≥ 60 at.% are highlighted by isoconcentration surfaces. Proximity histograms reveal that the carbon composition increases from 52 to > 80 at.% C, independent of the growth temperature. The average carbon composition underestimation by atom probe tomography reported here is related to detector dead time, since evaporation of carbon and carbon clusters is associated with multiple detection events that cannot be handled by the detector [42].

Fig. 3a shows a representative bright field transmission electron micrograph of the multinary carbide deposited at 873 K. The microstructure has columnar grains with widths typically between 5 and 15 nm. The high resolution micrographs shown in Fig. 3 (b&c) confirm that the samples are crystalline, with dense grain boundaries without voids.

Fig. 4 (a-c) highlight the high angle annular dark field (HAADF) micrographs of the samples deposited at 573, 873 and 1023 K. The darker regions are columnar grain boundaries which are regions of lower atomic density. The spotty contrast seen in higher magnification HAADF image (Fig. 4d) confirms that a uniform decoration of grain boundaries does not take place. In combination with dense grain boundaries and the observation of carbon-rich clusters seen from APT data (see Fig. 2), we speculate that the dark contrast regions are rich in carbon. Note that energy dispersive spectroscopy could not discern a clear carbon map. STEM-EDS shown in Fig. 4 e-h) reveals that the heavy elements are clearly depleted and non-uniformly distributed in the grain boundaries

The grain widths increase slightly (15–25 nm range) for the sample deposited at 1073 K compared to the one deposited at 573 K (5–10 nm).

3.3. Mechanical properties

Fig. 5a shows that the elastic modulus values measured from nanoindentation (range of 408 ± 4 to 325 ± 22 GPa) and microcantilever bending (range of 365 ± 33 to 314 ± 22 GPa) and the values are in very good agreement. The highest difference was found to be 15% for coatings deposited at 723 K. Note the inset in Fig. 5a displays a representative variation of the elastic modulus as a function of indentation depth. The presented values of elastic modulus and hardness are an average from an indentation depth range within 100 to 200 nm. Quasistatic indentations performed to a depth of 150 nm, virtually gave identical results. As visible from the inset, the elastic modulus decreases continuously with increasing indentation depths which can be understood by the increased contribution from the elastically compliant substrate.

In contrast, the elastic moduli obtained by microcantilever bending experiments do not have contributions from residual stresses or the compliant substrate. The data represents the elastic response averaging across the entire beam dimension. In both cases, the measured elastic modulus drops mildly with increasing deposition temperature. The fracture strengths (i.e. the failure stress in unnotched bending cantilevers assuming an Euler-Bernoulli cantilever) are reduced from 10.4 ± 3.5 GPa to 5.5 ± 0.4 GPa with increasing growth temperature (Fig. 5b). However, it is well known that fracture strengths of ceramics are subject to large stochastic uncertainty based on the underlying flaw distribution [43]. Therefore, a large number of tests need to be carried out to draw a conclusion with statistical certainty. The nanoindentation hardness values shown in Fig. 5 b) point to a substantial drop from 38.0 ± 1.8 GPa for coatings deposited at 723 K to 23.7 ± 3.3 GPa for those deposited at 1023 K. Conventionally, with increasing deposi-

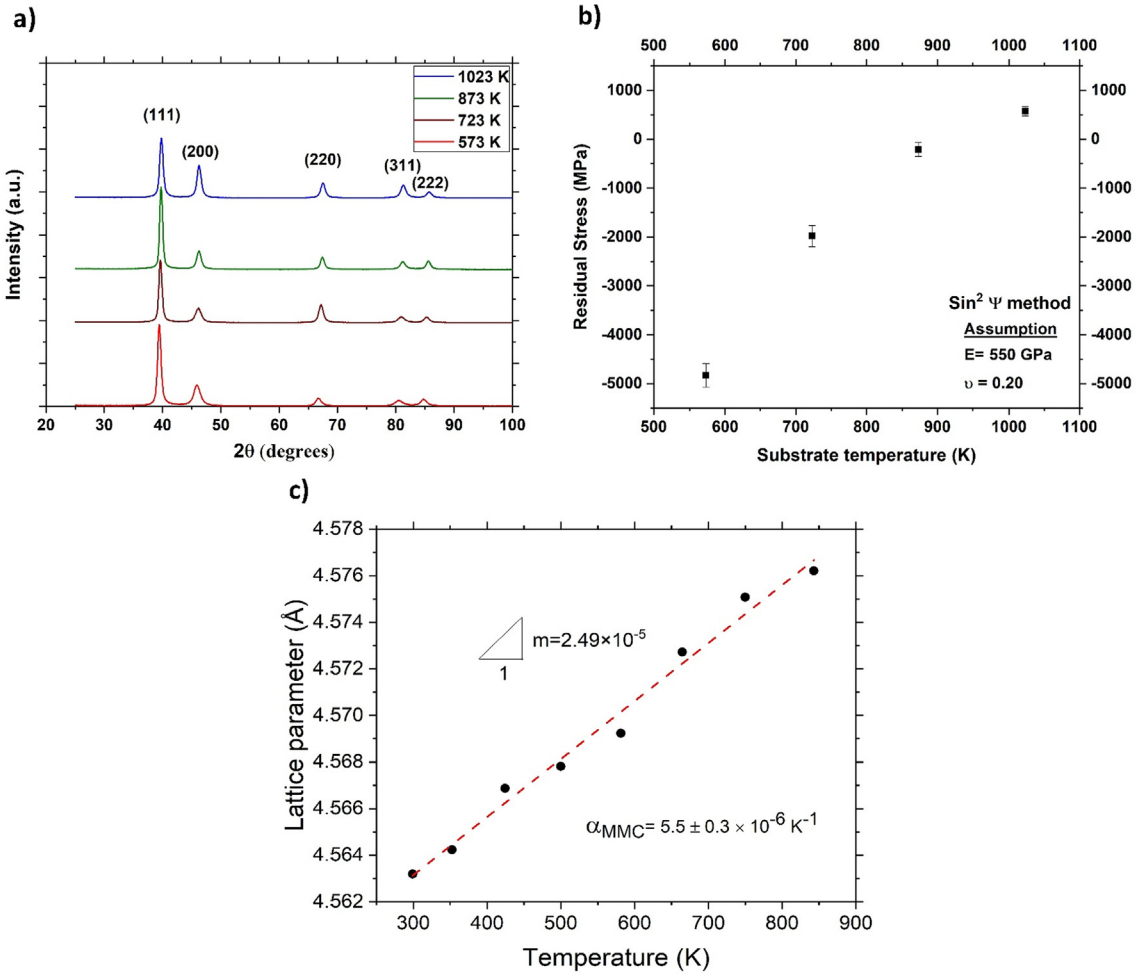

Fig. 1. a) X-ray diffractograms of the coatings deposited at different temperatures b) Residual stress determined as a function of deposition temperature c) Thermal expansion coefficient obtained from the stress free lattice parameters as a function of temperature.

tion temperatures for sputtered coatings, grains and grain boundaries are expected to be denser and closer to equilibrium conditions, therefore the elastic modulus and hardness are expected to increase [44]. Since the microstructure observably shows only a small increment in column size across deposition temperature, carbon enrichment at the column boundaries with increasing growth temperature appears to play a significant role in the mechanical property deterioration.

The measured residual stresses are substantially different and their role on the measured properties in conjunction with effect of the substrate on the measured nanoindentation properties will be discussed later in the manuscript. Linear elastic brittle fracture with high strength and hardness values suggest that there is high resistance to dislocation slip in these multi-metal carbides. Such high hardness could be linked to the ultra-fine grain widths of the columnar grains in the carbides, in addition to the solute strengthening effects in the metal sub-lattice. To ascertain the fracture toughness of these hard materials is a natural question that arises. Representative SEM images of the cube corner indentation imprints on coatings at different growth temperatures are shown in Fig. 6. The indentation stress intensity factor was calculated based on the equation (3) derived by Jang and Pharr [38].

It is clear from the images that radial cracks emanate from the corners of the indenter imprint. The radial cracks follow a wiggly path instead of being straight, suggesting that they are following the lower resistance column boundaries. The cracks also become prominent as the magnitude of the compressive residual stress decreases. The cracks are longest in extent (range of 1500–1800 nm) for the samples with tensile residual stress and short for the samples with the highest compressive stress (range of 420–470 nm). Correspondingly, the indentation stress intensity factor calculated (average values displayed in Fig. 6 a-d) is high for samples with high compressive residual stress and progressively decreases as residual stresses tend towards tensile character. Note that as the length of the cracks were a sizeable fraction of the coating thickness for the 1023 K sample, additional experiments were performed at a lower nominal displacement (200 nm), and these values were used for further calculation.

In order to assess the fracture toughness of coatings without residual stress, bending beams were fabricated with the help of FIB milling and tested with an *in situ* nanoindenter. The load displacement curves pointed to a linear elastic brittle fracture (shown in supplementary figure S3). The post mortem SEM images of the fractured surface shown in Fig. 7 across deposition temperatures are nominally straight with an orientation consistent with columnar grain boundaries. The post-mortem fracture surface images get progressively rougher with increasing deposition temperature. The fracture toughness values are nominally constant between 2.4 and 2.8 MPa.m$^{0.5}$ for all deposition temperatures except the one at 1023 K, for which the fracture toughness drops below 2 MPa.m$^{0.5}$ (average values displayed on Fig. 7 a-d). Both microcantilever and indentation measured toughness have crack paths along

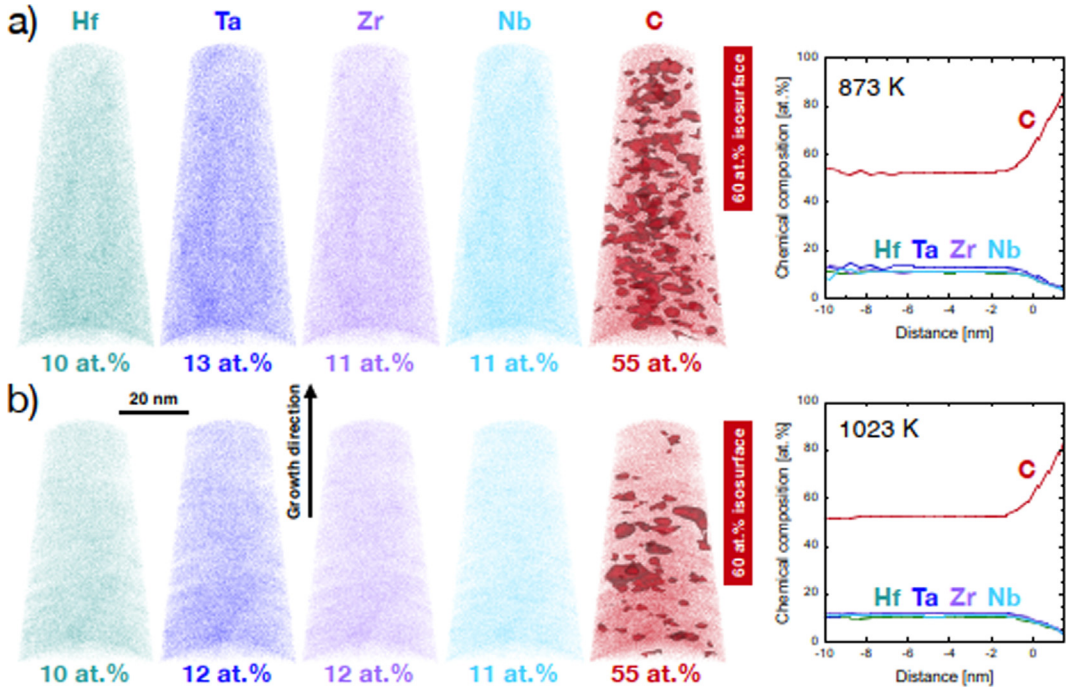

Fig. 2. Local chemical composition at the nanometer scale. Reconstructions of Hf, Ta, Zr, Nb and C are shown together with proximity histograms for C $\geq$ 60 at.% (reported as an average over all enriched clusters, the distance denotes deviation in composition away from the 60% concentration), for thin films grown at a) 873 K and b) 1023 K.

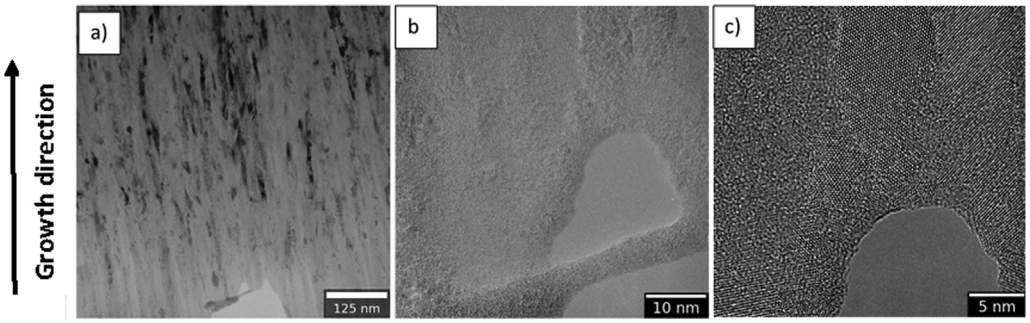

Fig. 3. a) Bright field transmission electron micrograph showing the nanostructure of the HfNbTaZr_C deposited at 873 K, b) & c) High resolution micrographs show crystalline grains, and dense grain boundaries.

columnar boundaries as suggested by fractography and accompanying APT measurements showing C-enrichment, and contrast changes at column boundaries in HAADF-STEM measurements, we speculate that columnar boundaries with enriched carbon are detrimental for the fracture toughness of multimetal carbide coatings.

The indentation induced stress intensity factor and the microcantilever based fracture toughness measurements are compiled in Fig. 8. For the sample deposited at 873 K two separate batches of cantilever fracture experiments separated by over a year in time were performed to check for repeatability. The average values have a difference of 12%.

Since, microcantilever experiments are very site specific, such small variations are reasonable across cantilever data sets. Also for this sample in an approximately residual stress-free state, the indentation and cantilever toughness values differ only by 8%. For samples deposited at lower temperature with compressive residual stresses, the indentation stress intensity factor is higher than cantilever toughness and vice-versa for the sample with tensile residual stress. The indentation induced stress intensity factor has a strong residual stress influence, and therefore it is not considered as fracture toughness. An approximate way to decouple the influence residual stress on fracture behavior, is to subtract the true cantilever measured fracture toughness from the apparent indentation toughness and plot against the product of residual stress and the square root of the indentation crack length. A linear relationship as observed in Fig. 8 b provides an estimate of the contribution of the residual stress towards the apparent toughness. The slope of the plot is the expected shape factor. However, nature and the magnitude of residual stress can influence the shape of the cracks. The shape of the cracks and their influence on the true indentation toughness will discussed in the following section. .

4. Discussion

4.1. Microstructure

Sputter deposition conditions strongly influence the microstructure of hard coatings. Based on Thornton's [44] original classification, sputtered coatings have a microstructure and morphology strongly dependent on the homologous temperatures of the material. For example, below a homologous temperature of

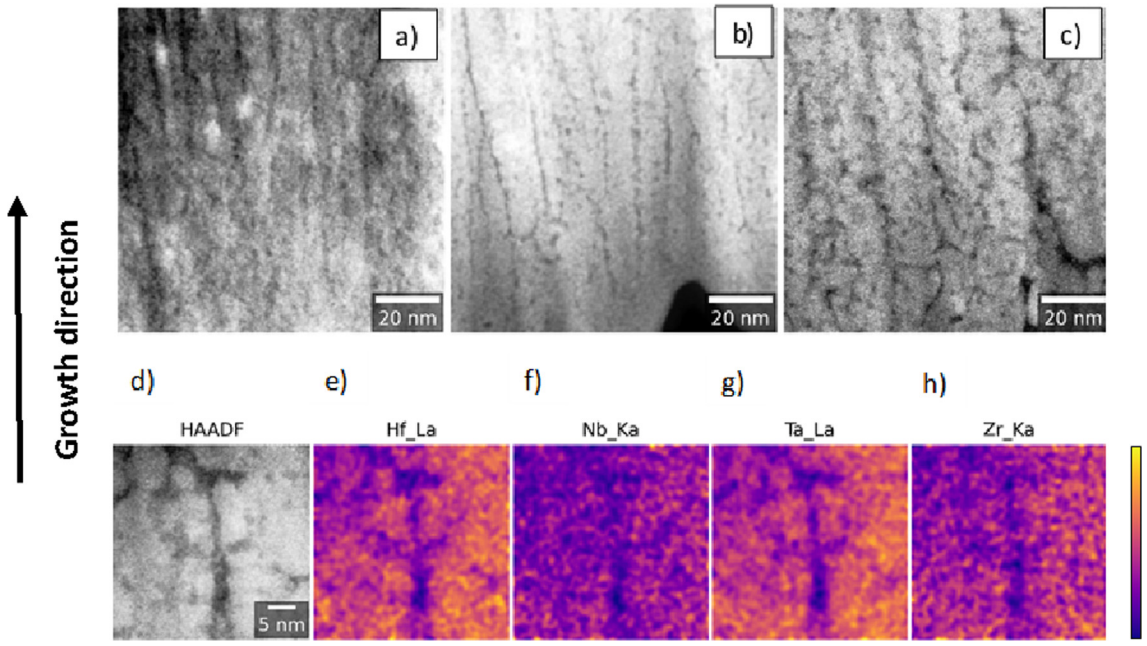

Fig. 4. A comparison of high angle annular dark field (HAADF) micrographs of coatings deposited at a) 573 K, b) 873 K and c) 1023 K. d) show a higher magnification HAADF image of the coating deposited at 873 K and e-h) shows the corresponding elemental distribution map obtained from energy dispersive spectroscopy in the scanning transmission electron microscopy mode (STEM). The colour legend shows changes in relative intensity in arbitrary units (dark blue: low concentration, bright yellow: high concentration). (For interpretation of the references to colour in this figure legend, the reader is referred to the web version of this article.)

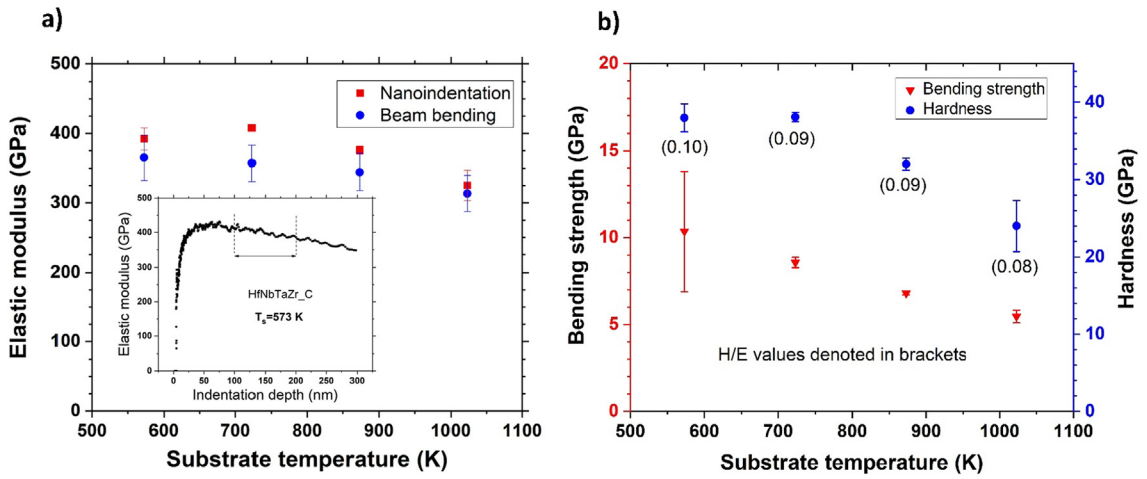

Fig. 5. a) Experimentally determined elastic modulus using microcantilever bending and nanoindentation. Inset: Representative curve showing elastic modulus variation with depth for HfNbTaZr_C deposited at 573 K, highlighting the depth range over which nanoindentation data are reported b) Fracture strength and hardness, from microcantilever bending and nanoindentation, respectively. Note that for some data points the error bars are smaller than the legend size.

0.1, low adatom mobility leads to porous grain boundaries. The homologous temperature of the coatings investigated here varies from 0.14 (573 K) to 0.26 (1023 K), assuming an effective melting temperature of 3973 K (based on equimolar fractions of ZrC, NbC, HfC and TaC). Therefore, for all deposition temperatures in this study the coating morphology is expected to be in Zone II with dense, pore-free grain boundaries. Structure zone diagrams also predict that with increasing growth temperature, grain boundaries become more compact, dense and strong. In case of TiN a transition from zone T to zone II has been observed for homologous temperatures between 0.21 and 0.26 [45]. The high-resolution bright field electron micrographs (Fig. 3) confirm that the column boundaries are dense and free of nanovoids. The growth of the carbon enriched clusters dispersed across the microstructure is seen through APT (Fig. 2) and preliminary evidence for carbon enrichment at columnar grain boundaries is seen in HAADF-STEM (Fig. 4). Further in-depth investigation is necessary to determine the grain boundary structures and nature of carbon enrichment at grain boundaries. It has been shown by *ab initio* calculations that HfC and especially TaC exhibit extremely small formation energies of carbon vacancies and carbon-deficient TaC_x and HfC_x ($x < 1$) are more stable than the stoichiometric carbides [1]. The increase in deposition temperature has been predicted to promote formation of carbon vacancies [1]. As the overall carbon content is not affected by the deposition temperature (see Table 1), the formation of carbon clusters from the excess carbon can thus be understood. In addition, increase in self-diffusion rates at higher temperatures may lead to Ostwald ripening in the carbon enriched second phase.

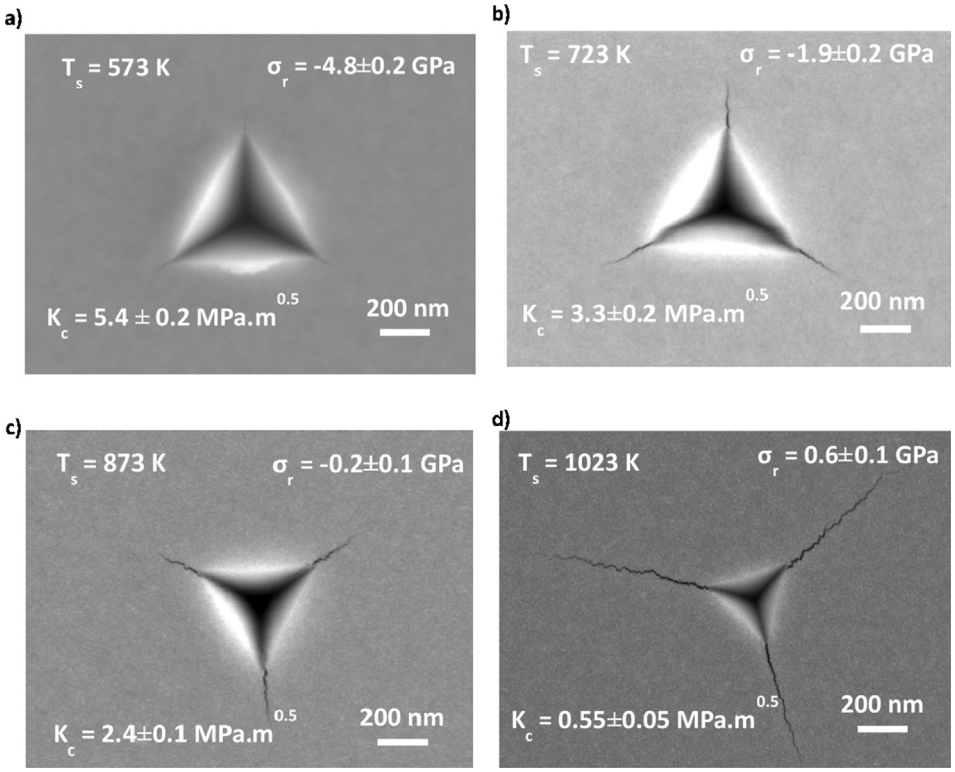

Fig. 6. Representative images of cube corner nanoindents used to measure the fracture toughness values with different residual stresses, with deposition temperatures, a) 573 K, b) 723 K, c) 873 K and d) 1023 K.

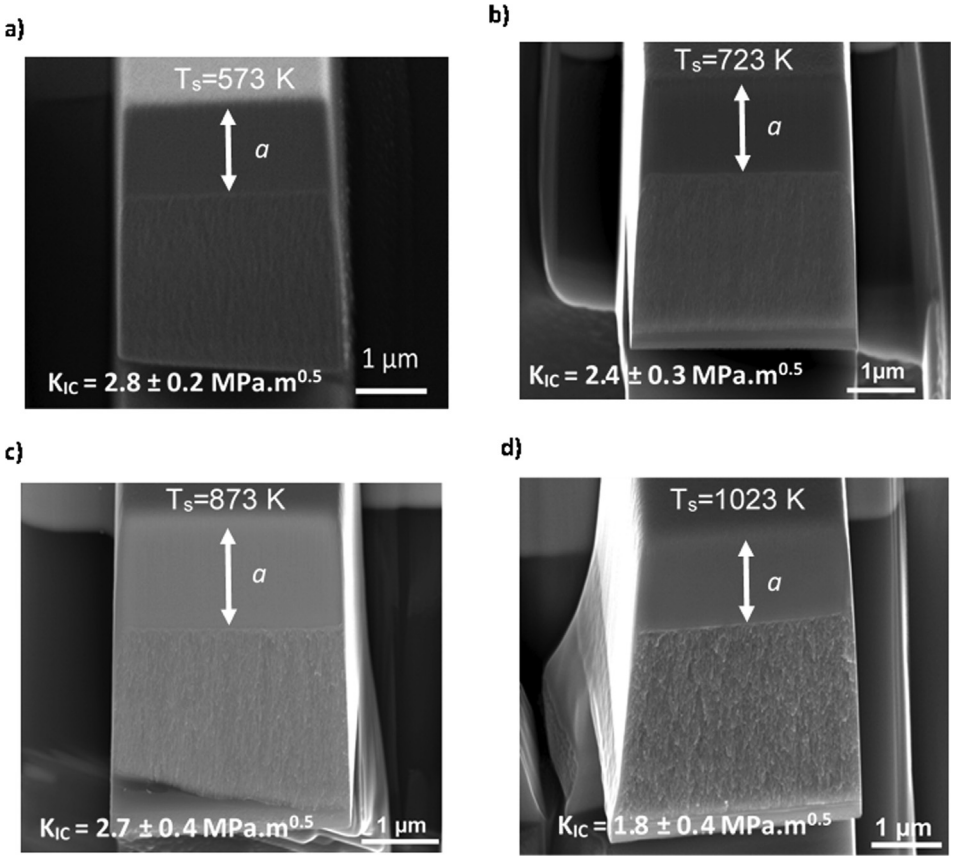

Fig. 7. Representative images of the fracture surface of notched microcantilevers deposited at different temperatures a) 573 K, b) 723 K, c) 873 K and d) 1023 K . (Note that the images were taken in an inclined view, the scale bar is valid only for the horizontal direction, additionally the ratio a/W is not affected by the tilt.)

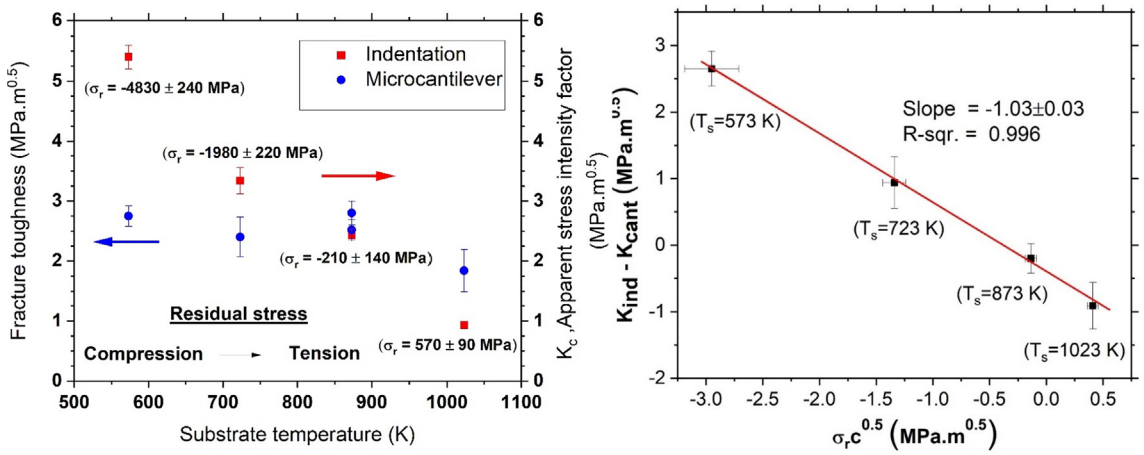

Fig. 8. a) Microcantilever and nanoindentation derived toughness data for all deposition temperatures. Note that for the sample deposited at 873 K, two sets of cantilever fracture toughness data were obtained to check for consistency in the data. b) Relationship between residual stress (σ_r) multiplied by square root of the indentation induced crack length (c) and apparent change in the toughness.

Table 1
Composition of the (HfNbTaZr)C as a function of deposition temperature.

Deposition Temperature (K)	Method	C (at%)	Hf (at%)	Ta (at%)	Nb (at%)	Zr (at%)
573	SEM-EDS	64.1 ± 9.8	8.5 ± 5.0	9.7 ± 1.7	8.5 ± 5	9.0 ± 5
723	SEM-EDS	65.8 ± 10.3	8.0 ± 7.3	9.3 ± 2.0	8.0 ± 5.7	8.9 ± 5.4
873	SEM-EDS	64.9 ± 10.1	8.2 ± 6.1	9.5 ± 1.9	8.3 ± 5.4	9.2 ± 5.2
	APT	54.8 ± 0.5	10.7 ± 0.3	12.8 ± 0.3	10.8 ± 0.3	11.0 ± 0.3
	ERDA	62.4 ± 1.3	18.6 ± 2.4*	19.0 ± 3.3*		
1023	SEM-EDS	64.6 ± 10.3	8.4 ± 7.4	9.7 ± 2.3	8.2 ± 5.8	9.2 ± 5.6
	APT	54.6	10.4	11.9	11.2	11.8

* Note: ERDA technique is unable to separate the contributions of individual adjoining heavy elements, therefore a joint composition value is reported.

4.2. Residual stress

As transition metal carbides possess high hardness and elastic modulus, plastic deformation cannot occur to relieve residual stresses arising in the coatings. In fully dense sputter deposited coatings, ion bombardment induced compressive residual stresses dominate for a variety of materials [46,47]. The thermal contribution to residual stress was estimated by considering the CTE mismatch between thin film and substrate. As seen from Fig. 1c, for the sample deposited at 873 K the CTE was determined to be 5.5 ± 0.3 × 10^{-6} K^{-1}. The microstructure and the composition are nominally similar for all the samples deposited at different growth temperatures, therefore, it is reasonable to assume that the CTE value remains unchanged. The silicon substrate and the silicon nitride barrier layer have very similar CTE values taken as 3.0 × 10^{-6} K^{-1} [46,48]. The magnitude of the thermal stresses in coating depends on the thermal expansion mismatch ($\Delta\alpha$), temperature difference (ΔT) and elastic properties (E taken from nanoindentation shown in Fig. 5a and ν taken as 0.2) of the film given by [46]

$$\Delta\sigma = \Delta T \times \Delta\alpha \times \frac{E}{(1-\nu)} \quad (5)$$

Therefore, when the multi-metal carbide coatings cool down from growth to room temperature, they are expected to develop significant tensile residual stress. Since the residual stresses are entirely elastic in nature in hard and stiff materials, the linear elastic superposition principle can be applied and the residual stress measured at room temperature is the net sum of the thermal and deposition-induced stresses. The magnitude of the thermally-induced tensile stress contribution for the sample deposited at 1023 K is of the order 660 MPa. The tensile residual stress measured for this sample is 570 ± 90 MPa. As the substrate temperature is increased from 573 K to 1023 K the corresponding homologous temperature increase from 0.14 to 0.26 indicated enhanced ad atom mobility which is expected to relax the sputtering induced compressive residual stresses. Therefore, at lower deposition temperatures residual stresses are compressive and gradually transition to have a tensile character. Note that the X-ray residual stress was only measured from the crystalline carbide phase, any additional potentially minor contribution from the carbon-rich clusters was not accounted.

4.3. Mechanical properties

4.3.1. Hardness and modulus

The multi-metal carbides offer the promise towards attaining super-hardness (H > 40 GPa), this has been demonstrated in (TiZrHfVNbTa)C coating deposited by gas phase reactive sputtering [17]. For the carbides deposited at 573 K, near super hardness of > 38 GPa was obtained as shown in Fig. 5b. The bulk hardness of the stoichiometric (HfNbTaZr)C carbide measured through nanoindentation is reported as 36.1 ± 1.6 GPa [32]. The combination of ultra-fine grains and solid solution effects in the metal sub-lattice should lead to further enhancements in the hardness of these multi-metal carbides in comparison with their bulk counterparts. However, Hossaini *et al.* [23] report that the presence of excess carbon above the stoichiometric limit has the effect of reducing the measured hardness.

The elastic modulus of the carbide coatings measured from nanoindentation and beam bending reported in Fig. 5a are clearly much lower (300–400 GPa) compared to 598 ± 15 GPa reported for the bulk (HfNbTaZr)C [32]. The elastic modulus measured by microcantilever bending is also slightly lower than the values mea-

sured by nanoindentation. It is likely that load frame compliance of the *in situ* nanoindenter, which was not corrected in the load displacement curves of the FIB milled un-notched cantilevers, may have resulted in the underestimation of the modulus values. The effect of compliant substrate becomes more prominent for the elastic modulus measurement as the indentation depth increases. Theoretical models and finite element simulations have been used to extract the elastic properties of the coatings by decoupling the elastic properties of the substrate [49–50]. However, these models are generally not applicable to coating-substrate systems with a modulus mismatch higher than a factor of 2.

Several studies through *in situ* SEM and TEM deformation of sputtered hard coatings have shown that indentation plasticity mechanistically occurs as a combination of grain boundary shear or column sliding, and dislocation plasticity in the ultrafine columnar grains [51–53]. Furthermore, Tilbrook *et al.* [51] show that for sputter deposited TiN, in addition to plastic deformation, radial, lateral and shear cracking are present as fracture mechanisms underneath the indenter. Therefore, as the growth temperature increases, the carbon enriched grain boundaries may facilitate easier column sliding, leading to a lowering of hardness and modulus. The decrease in bending fracture strength also noted with increasing growth temperatures follows a similar trend.

The residual stresses present in the coatings may affect the measured properties in two broad ways. Firstly, the intrinsic hardness and modulus measured could change due to residual stress. For example, Hans *et al.* [54] through *ab initio* density functional theory calculations and nanoindentation measurement show that the elastic modulus of TiAlN coatings, increase by nearly 11.5 GPa for an increment of 1 GPa compressive residual stress. Furthermore, Tilbrook *et al.* [51] through finite element simulations show the complex interplay of compressive residual stress, shear sliding and radial cracking in sputtered films. The equi-biaxial compressive residual stress acts normal to the column boundary and hinders shear sliding of the columnar boundaries, however a large increase in sliding stress may facilitate the intervention of radial cracking due to the tensile component of the indentation stress field. Secondly, systematic errors can be introduced in modulus and the hardness measurement in the Oliver-Pharr technique, in the presence of residual stresses. For example, Pharr and coworkers [55–56] demonstrate that a compressive residual stress of 300 MPa leads to an underestimation of the contact area up to 15 % in an aluminum alloy, resulting in an overestimation in the reported modulus and hardness. Plasticity generally relives residual stresses (in both tension and compression) in metallic materials with a relatively low resistance to dislocation slip, however, in hard coatings high compressive stresses do not lead to any plasticity, and high tensile stresses on the other hand lead to cracking. Therefore, a careful scrutiny of the effect of residual stress on the measured nanoindentation hardness and modulus is required for sputtered coatings.

4.3.2. Fracture toughness

Miniaturized mechanical testing for fracture toughness measurement has become fairly popular in the past decade [57–59]. In particular, notched microcantilevers fabricated by focused ion beam milling, coupled with *in situ* mechanical testing inside a SEM is widely adopted. The reliability of the fracture toughness measurement through this approach has been debated in considerable detail [57]. In particular, the role of a FIB cut starter notch, which lacks the ideal atomic sharpness of cracks, and thereby leading to an overestimation in the measurement toughness is widely discussed [60,61]. The chemical segregation of gallium to grain boundaries of selected materials [62], residual stresses in FIB-milled area [63] and the effect of ion current can change the notch root curvature [60], may impact the measured fracture toughness. However, in brittle materials, the FIB starter notch approximates well as a crack, as demonstrated by Jaya *et al.* [64] on silicon using different geometries. In particular, propagation of a sharp crack in stable test geometry (clamped beam bending) occurs at the same stress intensity as a FIB starter notch [64]. Therefore, the fracture toughness values reported from the notched microcantilever tests can be taken as the true toughness of the materials. The measured toughness values for the carbon-excess (HfNbTaZr)C coatings studied here lie in the range of 1.8–2.8 MPa.m$^{0.5}$ as seen in Fig. 8a. It is noteworthy, that the plastic zone size calculated for all the cases satisfy the plain strain fracture toughness criterion.

Pyramidal indentation based measurements have been formalized for estimation of fracture toughness of brittle materials for several decades [65,66]. Fracture mechanics formalisms based on the development of penny shaped cracks rely on a sound theoretical footing [67]. Pharr extended the approach to a three-sided cube corner indenter which displayed only radial cracking due to changes in the symmetry of the loading configuration [38]. Furthermore, their group addressed the problem to include short radial cracks to determine the reliability of the approach. Recently, Bruns et al. [68] showed that cube corner indentation based measurements were found to agree well with micropillar splitting fracture toughness values for fused quartz. The role of compressive residual stress in enhancing the effective toughness of brittle materials has been recognized as a design parameter for enhancing performance [21,69,70]. Klimashin *et al.* [71] directly plotted indentation stress intensity factor directly with residual stress, and reported an increment of 1.5 MPa.m$^{0.5}$ for 1 GPa increase in compressive residual stress. However, the explicit effect of residual stress on fracture toughness can be quantitatively decoupled as follows [72]:

$$K_{true} = K_c + Z \cdot \sigma_r c^{0.5} \tag{6}$$

Where, K_c is the stress intensity factor measured from indentation, K_{true} is the true indentation toughness, free from the influence of residual stress, Z is the shape factor and other terms were described earlier. The shape factor is generally assumed to be unaffected by the presence of the residual stress. To test that assumption and determine true indentation toughness, FIB cross-section were used to determine the depth of the crack *d* and the shape factor for each condition can be determined from the following expression [72].

$$Z = 1.12\sqrt{\pi}\frac{(d/c)}{(\frac{3\pi}{8}) + (\frac{\pi}{8}).(d/c)^2} \tag{7}$$

FIB cross sections presented in Fig. 9 a-d) allow the estimation of indentation crack depths. Cracks are shallower than their lengths with compressive residual stresses. Interestingly, the semi-circular (Z = 1.26) crack morphology is only approached in the presence of tensile residual stress. The nature and magnitude of the residual stress clearly affects the shape of the cracks, hence the shape factor and in turn the true toughness measurement as reported in Fig. 9e). True indentation toughness determined from equation (6), agrees very well with cantilever toughness, considering that is an independent technique. The true indentation toughness is consistently underestimated with respect to that obtained from cantilever bending. A maximum deviation of 25% was observed for the samples with a compressive residual stress of about 2 GPa. Notably, the error associated with indentation increases significantly as the magnitude of the residual stress increases. This is related to propagation of uncertainties, and relative errors add up in equation (6). Therefore, the cube corner indentation toughness testing technique can be a relatively quick benchmarking method for sputtered coatings. Note, the lower bound with the load thresholds for cracking even with sharp cube

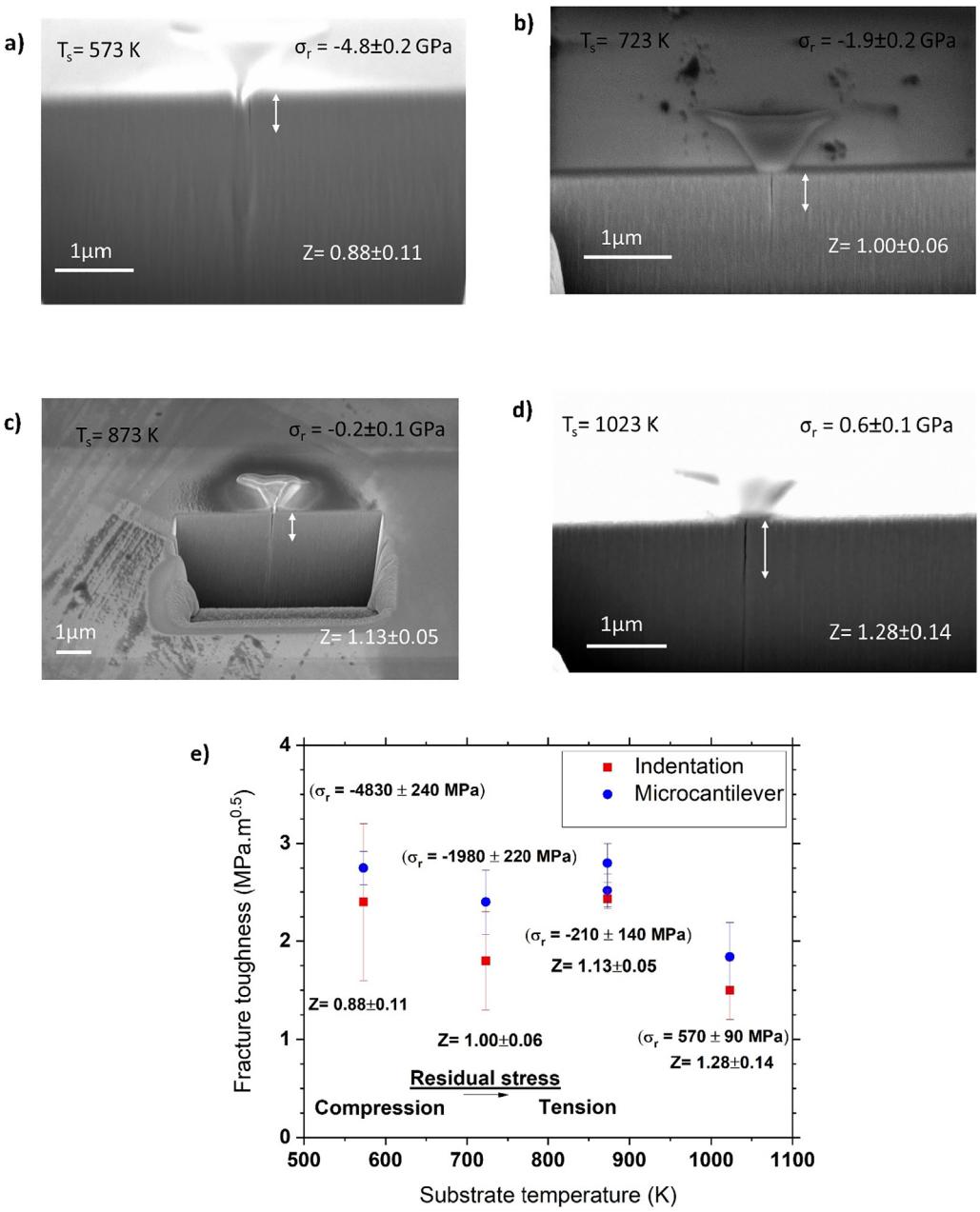

Fig. 9. a-d) FIB cross section of indents with different residual stresses arising from differences in deposition temperature and e) shows the comparison in the true toughness estimates measured by indentation and microcantilever bending.

corner indenters and upper bound displacement limitations, conventionally of the order of 10% of the film thickness restrict the range of applicability of the indentation technique.

The fracture toughness values reported here are comparable to that of TiN (2.0 MPa.m$^{0.5}$) and TiAlN (2.4 MPa.m$^{0.5}$) [73] and some sputtered high entropy nitrides (AlTaTiVZr)N and Si alloyed (AlTaTiVZr)N (2.4 MPa.m$^{0.5}$) [74]. Special nitride compositions are known to provide much higher estimates for fracture toughness [75]. Although to the best of the authors knowledge there are no reports of the fracture toughness measurements for multi-metal carbide sputtered coatings, some reports exist in their bulk counterparts. Vickers indentation based toughness estimates range from 3 to 8 MPa.m$^{0.5}$ [76]. A recent study by Casanadi *et al.* [77] with unnotched beam bending, used a non-standard indirect method obtained lower and upper bounds for individual grains of (HfNbTaZr)C and found a value between 2.4 and 4.5 MPa.m$^{0.5}$

4.3.3. Designing and testing approaches for multi-metal carbides:

Multi-metal carbides offer some of the same advantages as that of transition metal carbides, such as controlling carbon content to tailor properties. Furthermore, the solid solution hardening in the metal sub-lattice aids to promote hardness of the carbides. Clearly, the composition of the metals is expected to play a prominent role in determining the final mechanical properties. Recent progress in machine learning aided single phase carbide structures for materials discovery is fast developing into a new toolkit for the alloy carbides development [78]. On the experimental frontier, the use of combinatorial thin film experimental approaches can also be adopted to further this quest [79,80]. With the availability of a wide palette of material compositions, the need for accelerated mechanical testing then becomes essential for screening materials. Nanoindentation is ideally suited for this approach, not only to determine hardness and elastic modulus, but also with the

approach outlined in this manuscript to determine fracture toughness accurately. With such an approach, screened compositions can be subjected to more involved and rigourous mechanical testing approaches such as microcantilever test methods, which are otherwise time consuming.

Despite the enormous potential of some of these aforementioned methodologies for materials discovery, for sputtered hard coatings with nanocrystalline columnar grains, mechanical properties are ultimately governed by grain boundary fracture/failure. Therefore, any potential benefits of new materials discoveries could be stymied by premature failure in grain boundaries. For example, even in metallic NbMoTaW high entropy alloy films of grown by sputtering by Xiao *et al.* [81] the fracture toughness was 2.8–3.5 MPa.m$^{0.5}$, which is only modestly higher than the values reported in this study for the (HfNbTaZr)C hard coating. Additionally, the presence of excess carbon at the column grain boundaries may reduce the overall resistance to crack propagation, thereby reducing the fracture toughness. Optimizing carbon content and to keep it trapped within the grains is a possible way to promote grain boundary resistance. Furthermore, to mitigate the influence of columnar grain boundary failures, controlling morphologies of the interfaces in the sputtered films such promoting an equi-axed morphology, tilted grain boundary design [82] or amorphous coatings can be explored further [83].

5. Conclusion

An over-stoichiometric (HfNbTaZr)C multi-metal carbide coating with a crystalline phase and excess carbon clusters distributed through the structure was successfully deposited at different substrate temperatures. A nanocrystalline columnar morphology of the grains with carbon enrichment at grain boundaries accompanied by a modest increase in the grain size is observed with increasing substrate temperatures. A combination of near super hardness (38.0 ± 1.8 GPa) with respectable toughness values of 2.8 ± 0.2 MPa.m$^{0.5}$ were achieved in the coatings deposited at 573 K. For the coating deposited at the highest temperature (1023 K), the hardness and the fracture toughness dropped substantially to 25 ± 3.3 GPa and 1.8 ± 0.4 MPa.m$^{0.5}$, respectively. The CTE of these multi-element carbides was also determined to be 5.5 ± 0.3 × 10^{-6} K^{-1}. This was used to determine the thermal contribution to the residual stresses in coatings. The overall residual stresses were measured; specifically, their role on the fracture toughness was quantitatively determined experimentally. The presence of compressive residual stresses significantly improved the apparent fracture toughness and affects the shape of the indentation crack. The true indentation fracture toughness without the influence of the residual stress and microcantilever fracture toughness agree well. Microstructurally, the fracture in both the cantilever and the indentation experiment followed the grain boundary path. We speculate that the carbon enriched grain boundaries facilitate an easier crack propagation path and ultimately governing mechanical properties.

Data availability

Data will be made available on request.

Declaration of Competing Interest

The authors declare that they have no known competing financial interests or personal relationships that could have appeared to influence the work reported in this paper.

Acknowledgement

HG & GD gratefully acknowledge financial support from the German research foundation (Project DE 796/10-1)

Appendix A. Supplementary data

Supplementary data to this article can be found online at https://doi.org/10.1016/j.matdes.2022.111323.

References

[1] H. Lasfargues, T. Glechner, C.M. Koller, V. Paneta, D. Primetzhofer, S. Kolozsvári, D. Holec, H. Riedl, P.H. Mayrhofer, Non-reactively sputtered ultra-high temperature Hf-C and Ta-C coatings, Surf. Coat. Technol. 309 (2017) 436–444.
[2] T. Glechner, R. Hahn, L. Zauner, S. Rißlegger, A. Kirnbauer, P. Polcik, H. Riedl, Structure and mechanical properties of reactive and non-reactive sputter deposited WC based coatings, J. Alloys Compd. 885 (2021) 161129.
[3] W. Lengauer, "Transition metals carbides, nitrides and carbonitrides", Chapter 7, Handbook of ceramic hard materials, Wiley-VCH GmbH, 2000.
[4] T.Y. Kosolopova, Carbides: Properties, production and applications, Plenum press, New, 1971.
[5] "The chemistry of transition metal carbides and nitrides" edited by S.T. Oyama, Blackie academic and professional (1996) Glasgow
[6] Y. Xiao, J.-Y. Hwang, Y.-K. Sun, Transition metal carbide-based materials: synthesis and applications in electrochemical energy storage, J. Mater. Chem. A 4 (2016) 10379.
[7] Q.N. Meng, M. Wen, F. Mao, N. Nedfors, U. Jansson, W.T. Zheng, Deposition and characterization of reactive magnetron sputtered zirconium carbide films, Surf. Coat. Tech. 232 (2013) 876–883.
[8] C. Oses, C. Toher, S. Curtarolo, High entropy ceramics, Nat. Rev. Mater. 5 (2020) 295–309.
[9] S. Ranganathan, Alloyed pleasures: multimetallic cocktails, Curr. Sci. 85 (2003) 1403–1405.
[10] M.-H. Tsai, J.-W. Yeh, High entropy alloys: A critical review, Mater. Res. Lett. 2 (2014) 107–123.
[11] D.B. Miracle, O.N. Senkov, A critical review of high entropy alloys and related concepts, Acta Mater. 122 (2017) 448–511.
[12] E. Lewin, Multi-component and high-entropy nitride coatings: A promising field in need of a novel approach, J. Appl. Phys. 127 (2020) 160901.
[13] P.H. Mayrhofer, A. Kirnbauer, P.h. Ertelthaler, C.M. Koller, High-entropy ceramic thin films; A case study on transition metal diborides, Scr. Mater. 149C (2018) 93–97.
[14] U. Jansson, E. Lewin, Carbon-containing multi-component thin films, Thin Solid Films 688 (2019) 137411.
[15] A. Kirnbauer, A. Kretschmer, C.M. Koller, T. Wojcik, V. Paneta, M. Hans, J.M. Schneider, P. Polcik, P.H. Mayrhofer, "Mechanical properties and thermal stability of reactively sputtered multi-principal-metal Hf-Ta-Ti-V-Zr nitrides" Surf, Coat. Technol. 389 (2020) 125674.
[16] A. Kirnbauer, A. Wagner, V. Moraes, D. Primetzhofer, M. Hans, J.M. Schneider, P. Polcik, P.H. Mayrhofer, Thermal stability and mechanical properties of sputtered (Hf, Ta, V, W, Zr)-diborides, Acta Mater. 200 (2020) 559–569.
[17] V.F. Gorban, A.A. Andreyev, G.N. Kartmazov, A.M. Chikryzhov, M.V. Karpets, A. V. Dolomanov, A.A. Ostroverkh, E.V. Kantsyr, Production and mechanical properties of high_entropic carbide based on the TiZrHfVNbTa multicomponent alloy, J. Superhard mater. 39 (2017) 166–171.
[18] A. Kretschmer, A. Kirnbauer, E. Pitthan, D. Primetzhofer, K. Yalamanchili, H. Rudigier, Paul Heinz Mayrhofer "High-entropy alloy inspired development of compositionally complex superhard (Hf, Ta, Ti, V, Zr)-B-N coatings" Mater, Design 218 (2022) 110695.
[19] R.P. Thompson, W.J. Clegg, Predicting whether a material is ductile or brittle, Curr. Opinion solid state Mater. Sci. 22 (2018) 100–108.
[20] R. Soler, S. Gleich, C. Kirchlechner, C. Scheu, J.M. Schneider, G. Dehm, Fracture toughness of Mo2BC thin films: Intrinsic toughness versus system toughening, Mater. Design 154 (2018) 20–27.
[21] P. Malinovskis, S. Fritze, L. Riekehr, L. von Fieandt, J. Cedervall, D. Rehnlund, L. Nyholm, E. Lewin, U. Jansson, Synthesis and characterization of multicomponent (CrNbTaTiW)C films for increased hardness and corrosion resistance, Mater. Des. 149 (2018) 51–62.
[22] S. Fritze, P. Malinovskik, L. Riekehr, L. von Fieandt, E. Lewin, U. Jansson, Hard and crack resistant carbon supersaturated refractory nanostructured multicomponent coatings, Sci. Rep. 8 (2018) 14508.
[23] M.D. Hossain, T. Borman, A. Kumarb, X. Chen, A. Khosravani, S.R. Kalidindi, E.A. Paisley, M. Esters, C. Oses, C. Toher, S. Curtarolo, J.M. LeBeau, D. Brenner, J.-P. Maria, Carbon stoichiometry and mechanical properties of high entropy carbides, Acta Mater. 215 (2021) 117051.
[24] T.W. Scharf, H. Deng, J.A. Barnard, Mechanical and fracture toughness studies of amorphous SiC–N hard coatings using nanoindentation, J. Vac. Sci. Tech. A 15 (1997) 963–967.
[25] K.I. Schiffmann, Determination of fracture toughness of bulk materials and thin films by nanoindentation: comparison of different models, Phil. Mag. 91 (2011) 1163–1178.

[26] Q. Wang, F. Zhou, Q. Ma, M. Callisti, T. Polcar, J. Yan, "Fracture toughness and sliding properties of magnetron sputtered CrBC and CrBCN coatings" Appl, Surf. Sci. 443 (2018) 635–643.
[27] W.S. Williams, Transition metal carbides, Prog. Solid State Chem. 6 (1971) 57–118.
[28] G. Bilger, T. Voss, T. Schlenker, A. Strohm, High temperature diffusion barriers from Si-rich Silicon-nitride, Surf. Interface Anal. 38 (2006) 1687–1691.
[29] Y. Shirotori, K. Sawada, K. Ozawa, K. Edamoto, S. Otani, Photoelectron Spectroscopy Study of the Oxidation of TiC(100), Jpn. J. Appl. Phys. 42 (2003) 1725–1731.
[30] G. Nolze, R. Hielscher, Orientations - perfectly coloured, J. Appl. Crystallogr. 49 (2016) 1786–1802.
[31] M.E. Hilley, Residual stress measurement by X-ray diffraction, Soc. Automoti. Eng. J784a (1971) 20.
[32] E. Castle, T. Csanádi, S. Grasso, J. Dusza, M. Reece, "Processing and properties of high-entropy ultra-high temperature carbides" Sci, Rep. 8 (2018) 8609.
[33] C. Kral, W. Lengauer, D. Rafaja, P. Ettmayer, Critical review on the elastic properties of transition metal carbides, nitrides and carbonitrides, J. alloys compnds. 265 (1998) 215–233.
[34] Y. Zhang, H.J. Whitlow, T. Winzell, I.F. Bubb, T. Sajaraava, K. Arstila, J. Keinonen, Detection efficiency of time-of-flight energy elastic recoil detection analysis system, Nucl. Instrum. Methods Phys. Res. Sec. B 149 (1999) 477–489.
[35] M.S. Janson, CONTES (Conversion of Time-Energy Spectra), a Program for ERDA Data Analysis, Uppsala University, 2004. Internal Report,.
[36] K. Thompson, D. Lawrence, D.J. Larson, J.D. Olson, T.F. Kelly, B. Gorman, In situ site-specific specimen preparation for atom probe tomography, Ultramicroscopy 107 (2007) 131–139.
[37] G.M. Pharr, Measurement of mechanical properties by ultra-low load indentation, Mater. Sci. Eng. A 253 (1998) 151–159.
[38] J. Jang, G.M. Pharr, Influence of indenter angle on cracking in Si and Ge during nanoindentation, Acta Mater. 56 (2008) 4458–4469.
[39] S. Brinckmann, K. Matoy, C. Kirchlechner, G. Dehm, On the influence of microcantilever pre-crack geometries on the apparent fracture toughness of brittle materials, Acta Mater. 136 (2017) 281–287.
[40] K. Matoy, H. Schönherr, T. Detzel, T. Schöberl, R. Pippan, C. Motz, G. Dehm, A comparative microcantilever study of the mechanical behavior of silicon based passivation films, Thin Solid Films 518 (2009) 247–256.
[41] S. Brinckmann, C. Kirchlechner, G. Dehm, Stress intensity factor dependence on anisotropy and geometry during micro-fracture experiments, Scr. Mater. 127 (2017) 76–78.
[42] M. Thuvander, J. Weidow, J. Angseryd, L.K.L. Falk, F. Liu, M. Sonestedt, K. Stiller, H.-O. Andrén, Quantitative atom probe analysis of carbides, Ultramicroscopy 111 (2011) 604–608.
[43] M.W. Barsoum, Fundamentals of ceramics, Taylor & Francis group, 2003.
[44] J.A. Thornton, Influence of apparatus geometry and deposition conditions on the structure and topography of thick sputtered coatings, J. Vac. Sci. Tech. 11 (1974) 666.
[45] M.K. Hibbs, B.O. Johansson, J.-E. Sundgren, U. Helmersson, Effects of substrate temperature and substrate material on the structure of reactively sputtered TiN films, Thin Solid Films 122 (1984) 115–129.
[46] L.B. Freund, S. Suresh, Thin film materials: Stress, defect formation and surface evolution, Cambridge University Press, 2003.
[47] S.J. Bull, A.M. Jones, A.R. McCabe, Residual stress in ion-assisted coatings, Sur. Coat. Tech. 54 (55) (1992) 173–179.
[48] C.-L. Tien, T.-W. Lin, Thermal expansion coefficient and thermomechanical properties of SiN_x thin films prepared by plasma-enhanced chemical vapor deposition, Appl. Opt. 51 (2012) 7229–7235.
[49] J. Hay, B. Crawford, Measuring substrate-independent modulus of thin films, J. Mater. Res. 26 (2011) 727–738.
[50] S.J. Bull, A simple method for the assessment of the contact modulus for coated systems, Philos. Mag. 95 (2015) 1907–1927.
[51] M.T. Tilbrook, D.J. Paton, Z. Xie, M. Hoffman, Microstructural effects on indentation failure mechanisms in TiN coatings: Finite element simulations, Acta Mater. 55 (2007) 2489–2501.
[52] L.W. Ma, J.M. Cairney, M. Hoffman, P.R. Munroe, Deformation mechanisms operating during nanoindentation of TiN coatings on steel substrates, Surf. Coat. Tech. 192 (2005) 11–18.
[53] K. Rzepiejewska-Malyska, M. Parlinska-Wojtan, K. Wasmer, K. Hejduk, J. Michler, *In-situ* SEM indentation studies of the deformation mechanisms in TiN, CrN and TiN/CrN, Micron 40 (2009) 22–27.
[54] M. Hans, L. Patterer, D. Music, D.M. Holzapfel, S. Evertz, V. Schnabel, B. Stelzer, D. Primetzhofer, B. Völker, B. Widrig, A.O. Eriksson, J. Ramm, M. Arndt, H. Rudigier, J.M. Schneider, Stress-Dependent Elasticity of TiAlN Coatings, Coatings 9 (2019) 24.
[55] T.Y. Tsui, W.C. Oliver, G.M. Pharr, Influences of stress on the measurement of mechanical properties using nanoindentation: Part I. Experimental studies in an aluminum alloy, J. Mater. Res. 11 (1996) 752–759.
[56] A. Bolshakov, W.C. Oliver, G.M. Pharr, Influences of stress on the measurement of mechanical properties using nanoindentation: Part II. Finite element simulations, J. Mater. Res. 11 (1996) 760–768.
[57] G. Dehm, B.N. Jaya, R. Raghavan, C. Kirchlechner, Overview on micro- and nanomechanical testing: New insights in interface plasticity and fracture at small length scales, Acta Mater. 142 (2018) 248–282.
[58] J. Ast, M. Ghidelli, K. Durst, M. Göken, M. Sebastiani, A.M. Korsunsky, "A review of experimental approaches to fracture toughness evaluation at the micro-scale" Mater, Design 173 (2019) 107762.
[59] R. Pippan, S. Wurster, D. Kiener, Fracture mechanics of micro samples: Fundamental considerations, Mater. Design 159 (2018) 252–267.
[60] J.P. Best, J. Zechner, J.M. Wheeler, R. Schoeppner, M. Morstein, J. Michler, Small-scale fracture toughness of ceramic thin films: the effects of specimen geometry, ion beam notching and high temperature on chromium nitride toughness evaluation, Phil. Mag. 96 (2016) 3552–3569.
[61] S. Wurster, C. Motz, R. Pippan, Characterization of the fracture toughness of micro-sized tungsten single crystal notched specimens, Phil. Mag. 92 (2012) 1803–1825.
[62] Y. Xiao, V Maier-Kiener, J. Michler, R. Spolenak, J.M. Wheeler, Deformation behavior of aluminum pillars produced by Xe and Ga focused ion beams: Insights from strain rate jump tests, Mater Design, 181 (2019) 107914
[63] C.M. Lauener, L. Petho, M. Chen, Y. Xiao, J. Michler, J.M. Wheeler, Fracture of Silicon: Influence of rate, positioning accuracy, FIB machining, and elevated temperatures on toughness measured by pillar indentation splitting, Mater. Design 142 (2018) 340–349.
[64] B.N. Jaya, C. Kirchlechner, G. Dehm, Can microscale fracture tests provide reliable fracture toughness values? A case study in silicon, J. Mater. Res. 30 (2015) 686–698.
[65] G.R. Anstis, P. Chantikul, B.R. Lawn, D.B. Marshall, A critical evaluation of indentation techniques for measuring fracture toughness: I, direct crack measurements, J. Am. Ceram. Soc. 64 (1981) 533–538.
[66] P. Ostojic, R. McPherson, A review of indentation fracture theory: its development, principles and limitations, Inter. J. Fracture 33 (1987) 297–312.
[67] B.R. Lawn, E.R. Fuller, Equilibrium penny-like cracks in indentation fracture, J. Mater. Sci. 10 (1975) 2016–2024.
[68] S. Bruns, L. Petho, C. Minnert, J. Michler, K. Durst, Fracture toughness determination of fused silica by cube corner indentation cracking and pillar splitting, Materials and Design 186 (2020) 108311.
[69] D.B. Marshall, B.R. Lawn, An indentation technique for measuring stresses in tempered glass surfaces, J. Am. Ceram. Soc. 60 (1976) 86–87.
[70] J. Buchinger, L. Löfler, J. Ast, A. Wagner, Z. Chen, J. Michler, Z.L. Zhang, P.H. Mayrhofer, D. Holec, M. Bartosik, Fracture properties of thin film TiN at elevated temperatures, Mater. Design 194 (2020) 108885.
[71] F.F. Klimashin, L. Lobmaier, N. Koutná, D. Holec, P.H. Mayrhofer, "The MoN–TaN system: Role of vacancies in phase stability and mechanical properties" Mater, Design 202 (2021) 109568.
[72] J. Chen, Indentation-based methods to assess fracture toughness for thin coatings, J. Phys. D: Appl. Phys. 45 (2012) 203001.
[73] M. Bartosik, C. Rumeau, R. Hahn, Z.L. Zhang, P.H. Mayrhofer, "Fracture toughness and structural evolution in the TiAlN system upon annealing" Sci, Rep. 7 (2017) 16476.
[74] R. Hahn, A. Kirnbauer, M. Bartosik, S. Kolozsvári, P.H. Mayrhofer, Toughness of Si alloyed high-entropy nitride coatings, Mater. Lett. 251 (2019) 238–240.
[75] W.M. Seidl, M. Bartosika, S. Kolozsvári, H. Bolvardi, P.H. Mayrhofer, Influence of Ta on the fracture toughness of arc evaporated Ti-Al-N, Vac. 150 (2018) 24–28.
[76] C. Peng, X. Gao, M. Wang, L. Wu, H. Tang, X. Li, Q. Zhang, Y. Ren, F. Zhang, Y. Wang, B. Zhang, B. Gao, Q. Zou, Y. Zhao, Q. Yang, D. Tian, H. Xiao, H. Gou, W. Yang, X. Bai, W.L. Mao, H-k. Mao, Diffusion-controlled alloying of single-phase multi-principal transition metal carbides with high toughness and low thermal diffusivity, Appl. Phys. Lett. 114 (2019) 011905.
[77] T. Csanadia, M. Vojtkoa, Z. Dankhazib, M.J. Reece, J. Dusza, Small scale fracture and strength of high-entropy carbide grains during microcantilever bending experiments, J. Euro. Ceram. Soc. 40 (2020) 4774–4782.
[78] K. Kaufmann, D. Maryanovsky, W.M. Mellor, C. Zhu, A.S. Rosengarten, T.J. Harrington, C. Oses, C. Toher, S. Curtarolo, K.S. Vecchio, Discovery of high-entropy ceramics via machine learning, Computational Mater. 42 (2020) 1–9.
[79] T. Gebhardt, D. Music, T. Takahashi, J.M. Schneider, Combinatorial thin film materials science: From alloy discovery and optimization to alloy design, Thin Solid Films 520 (2012) 5491–5499.
[80] A. Ludwig, Discovery of new materials using combinatorial synthesis and high-throughput characterization of thin-film materials libraries combined with computational methods, npj Computational Mater. (2019) 70.
[81] Y. Xiao, Y. Zoub, H. Ma, A.S. Sologubenko, X. Maeder, R. Spolenak, J.M. Wheeler, Nanostructured NbMoTaW high entropy alloy thin films: High strength and enhanced fracture toughness, Scr. Mater. 168 (2019) 51–55.
[82] R. Daniel, M. Meindlhumer, W. Baumegger, J. Zalesak, B. Sartory, M. Burghammer, C. Mitterer, J. Keckes, Grain boundary design of thin films: Using tilted brittle interfaces for multiple crack deflection toughening, Acta Mater. 122 (2017) 130–137.
[83] B. Völker, B. Stelzer, S. Mráz, H. Rueß, R. Sahu, C. Kirchlechner, G. Dehm, J.M. Schneider, On the fracture behavior of Cr_2AlC coatings, Mater. Design 206 (2021) 109757.